European Congress on Computational Methods
in Applied Sciences and Engineering (ECCOMAS 2012)
J. Eberhardsteiner et.al. (eds.)
Vienna, Austria, September 10-14, 2012

LINEAR FREQUENCY DOMAIN PREDICTIONS OF DYNAMIC DERIVATIVES FOR THE DLR F12 WIND TUNNEL MODEL

M. Widhalm[1], A. R. Hübner[1], and R. Thormann[2]

[1]German Aerospace Center (DLR), Institute of Aerodynamics and Flow Technology.
Lilienthalplatz 7, 38108 Braunschweig.
e-mail: {markus.widhalm,andreas.huebner}@dlr.de

[2] German Aerospace Center (DLR), Institute of Aeroelasticity,
Bunsenstr. 10, 37073 Göttingen
e-mail: reik.thormann@dlr.de

Keywords: unsteady aerodynamics, flutter analysis, linearization, frequency domain

Abstract. *Structural loads for full aircraft configurations can be represented by evaluating dynamic derivatives over a wide parameter space mainly including different mode shapes, angle of attack and Mach numbers. Traditionally, these values are determined by wind tunnel tests applying forced periodic motions to aircraft models. The ability of numerical simulations provide an excellent addendum to wind tunnel tests. Instead of time-accurate unsteady Reynolds-averaged Navier-Stokes (URANS) solvers which are recognized as extremely computational expensive this paper considers a linearized frequency domain solver (LFD). With this approach the unsteady simulation reduces to a single steady state computation and a single linear simulation in the frequency domain. By the assumption of small perturbations and harmonic oscillations dynamic derivatives can be computed efficiently within a wide parameter space. In addition, the theoretical background for the LFD will be presented. Based on the linearization of the RANS equations and modeling of small perturbations with Fourier series a complex valued linear system has to be solved.*

1 INTRODUCTION

The dynamic derivatives are determined to study the aircrafts flight dynamics. This is an essential part in the design phase. Stability analysis includes many different structural loadings and flow conditions, such as an interception (flare) maneuver with increased load factors. Furthermore, particularly in transonic regions an aircraft with elastic wings may undergo the aeroelastic effect flutter. This situation is especially severe for swept-back wings since they experience a sharp drop of the flutter (stability) boundary called transonic dip [25, 15].
Flutter is caused by interaction between aerodynamic and elastic internal structural loads. This can result in a damage of components, destruction of an entire aircraft or cause structural fatigue. In that sense the sizing of an aircraft and its flight control needs to be designed well beyond critical flight situations. Therefore, the estimation of dynamic derivatives will place special attention.
As a consequence, since the beginning of the last century an intensive research on the understanding of flight dynamics in connection with elastic aircrafts has started. Various factors of nonlinear aeroelasticity are taking place, summarized by Dowell [6], like aerodynamic shocks, flow separation, generation of vortices and on the structural part geometric deformations, friction and freeplay.
Despite all the progress which has been achieved so far, this analysis is still a time intensive research today. There is not only an immensely large parameter range to be covered, including Mach number, density, altitude, frequencies, deformation amplitudes and structural modes. It is further relevant to provide results in a certain short amount of time, which is not guaranteed for all numerical methods. Furthermore, through increasing interest in multi disciplinary optimization (MDO), it becomes more and more important to account for accurate dynamic derivatives at early design stages. This may reduce the possibility of expensive re-engineering, too.
Half a century ago, particularly computational efficient methods based on the potential theory, i.e. Doublet Lattice methods (DLM) [1, 10, 9, 5], were the backbone for many studies of aeroelastic effects, especially for flutter analysis. Since three decades other numerical methods, at first based on the transonic small perturbation (TSP) equations [16, 29] and later on Euler [3] and Navier-Stokes equations [34], have matured to a promising prediction tool and used continuously for many flow applications. But unfortunately, they were lacking behind, in contrast to DLM, because of their costly computation time. Nevertheless, to speed up the prediction for flutter boundaries, alternative methods like linearized techniques based on Euler and Navier-Stokes equations have received special attention. These methods prospect to reduce the computational effort by at least an order of magnitude only by a certain loss of generality in comparison to full time-accurate unsteady flow simulations. These methods were initially limited to inviscid flows [24, 11, 32]. But after continuous developments calculations with a linearized viscous approach [20, 26, 33, 2, 14] seem to be promising to capture accurately nonlinear flow effects, like shocks and flow separation.
The paper will present a brief overview of the applied numerical method. The capability of predicting dynamic derivatives with the LFD approach are examined with the DLR F12 wind tunnel model [13, 23]. Experimental data and DLM results from the DLR F12 are compared to numerical time-accurate unsteady as well as LFD results for viscous flow conditions.

2 THE LINEARZED FREQUENCY DOMAIN SOLVER

At first we will describe the governing equations for a viscous fluid flow and subsequently derive the discretized equations solved with an iterative time integration scheme. The equations for the linearized frequency domain solver are then obtained by linearization of the discretized system of flow equations.

2.1 Governing equations

The considered equations are the mass-weighted (Favre) averaged three-dimensional unsteady Navier-Stokes equations with a Spalart-Allmaras one equation turbulence model [30]. They may be written for an open physical domain $\Omega(t) \subset \mathbb{R}^3$ enclosed by a smooth boundary $\partial\Omega(t)$ under the time-dependent coordinate $\mathbf{x}(t)$ within a velocity field of

$$\begin{aligned} \mathbf{U}(\mathbf{x}(t),t) &= \left[u(\mathbf{x},t), v(\mathbf{x},t), w(\mathbf{x},t)\right]^T, \\ \mathbf{x}(t) &= \left[x(t), y(t), z(t)\right]^T \end{aligned} \tag{1}$$

in integral and conservative form like

$$\frac{\mathrm{d}}{\mathrm{d}t}\int_{\Omega(t)} \mathbf{W}\,\mathrm{d}|\Omega| + \int_{\partial\Omega(t)} \left(\mathbf{f}_c\cdot\mathbf{n} - \mathbf{f}_v\cdot\mathbf{n} - \mathbf{W}\,\dot{\mathbf{x}}\cdot\mathbf{n}\right)\mathrm{d}|\partial\Omega| = \int_{\Omega(t)} \mathbf{Q}\,\mathrm{d}|\Omega| \tag{2}$$

where $\mathbf{W}$ is the conservative state variables vector

$$\mathbf{W} := \left[\rho, \rho u, \rho v, \rho w, \rho E, \rho\tilde{\nu}\right]^T. \tag{3}$$

and $\mathbf{n}$ denotes the time dependent normal vector. In addition, grid point velocities $\dot{\mathbf{x}} := \dot{\mathbf{x}}(\mathbf{x}(t))$ appear. The flux density vectors of convective $\mathbf{f}_c$ and viscous $\mathbf{f}_v$ fluxes are given by:

$$\mathbf{f}_c\cdot\mathbf{n} = \begin{bmatrix} \rho V_n \\ \rho u V_n + p n_x \\ \rho v V_n + p n_y \\ \rho w V_n + p n_z \\ \rho H V_n \\ \rho\tilde{\nu} V_n \end{bmatrix}, \quad \mathbf{f}_v\cdot\mathbf{n} = \begin{bmatrix} 0 \\ \tau_{xj} \\ \tau_{yj} \\ \tau_{zj} \\ \Theta_j \\ \tau_j^t \end{bmatrix}\cdot\mathbf{n} \tag{4}$$

including $V_n = \langle\mathbf{U},\mathbf{n}\rangle$ the normal velocity over interface $\partial\Omega(t)$. Assuming a calorically perfect gas, the relation between the static pressure and temperature follows from the equation of state $p/\rho := \mathcal{R}T$, $\mathcal{R}$ is the specific gas constant, which closes the system. With the total enthalpy H and the relationship between static pressure and state variables by

$$H := E + p/\rho, \quad p := (\gamma-1)\rho\left(E - \frac{|\mathbf{U}|^2}{2}\right) \tag{5}$$

the specific total energy E can be described. Detailed expressions for the viscous density fluxes introducing the viscous shear-stress tensor $\tau($**U** and corresponding viscous energy Θ can be found in more detail in Ref.[31]. The source term $\mathbf{Q}$ occurring on the right hand side of (2) can be further split into

$$\mathbf{Q}(\mathbf{x},t) = \mathbf{Pr}(\mathbf{x},t) - \mathbf{De}(\mathbf{x},t) - \mathbf{Di}(\mathbf{x},t) \tag{6}$$

where $\mathbf{Pr}$ corresponds to production, $\mathbf{De}$ is destruction and $\mathbf{Di}$ is the non-conservative diffusion term. These three terms are then deduced by the particular turbulence model used, in that case Spalart-Allmaras one equation model.

The boundary conditions imposed for viscous walls are:

$$u(\mathbf{x},t) = v(\mathbf{x},t) = v(\mathbf{x},t) = 0 \tag{7}$$

For initial conditions the flow field is initialized with free stream quantities derived from Mach number and Reynolds number. In addition to complete the system reference Sutherland's temperature is taken to be 273.15 Kelvin.

2.2 Finite volume discretization

Applying an unstructured edge based cell-vertex finite-volume discretization, (2) is solved using a spatial central numerical flux to compute the residual $\mathbf{R}$

$$\mathbf{R}(\mathbf{W}(\mathbf{x},\dot{\mathbf{x}})) := \int_{\partial\Omega(t)} (\mathbf{f}_c \cdot \mathbf{n} - \mathbf{f}_v \cdot \mathbf{n} - \mathbf{W}\,\dot{\mathbf{x}} \cdot \mathbf{n})\,\mathrm{d}|\partial\Omega| - \int_{\Omega(t)} \mathbf{Q}\,\mathrm{d}|\Omega| \tag{8}$$

with mixed second and fourth order dissipation operators after the scheme of Jameson, Schmidt, Turkel (JST) [17]. The convective flux $\mathbf{f}_c$ over an interface $\partial\Omega(t)$ of a control volume $\Omega(t)$, which are formed by a median dual grid approach, is written

$$\mathbf{f}_{c,JST} \cdot \mathbf{n}_{ij} = \frac{1}{2}(\mathbf{f}_c(\mathbf{W}_i) \cdot \mathbf{n}_{ij} + \mathbf{f}(\mathbf{W}_j)_c \cdot \mathbf{n}_{ij}) - \frac{1}{2}|\mathbf{A}_{ij}|[\mathbf{W}_i - \mathbf{W}_j] \tag{9}$$

where $|\mathbf{A}_{ij}|$ is in case of scalar dissipation the maximum absolute convective eigenvalue. The neighbors of point i are described by $N(i)$ and the face between the points i and j is ij with its adjacent normal vector $\mathbf{n}_{ij}$. Artificial dissipation is added with expression $[\mathbf{W}_i - \mathbf{W}_j] = \mathbf{D}_{ij}$ and is computed as

$$\mathbf{D}_{ij} = \phi_2(\mathbf{W}_j - \mathbf{W}_i) - \phi_4(L_j(\mathbf{W}) - L_i(\mathbf{W})) \tag{10}$$

$$\text{and } L_i(\mathbf{W}) = \sum_{j \in N(i)} (\mathbf{W}_j - \mathbf{W}_i). \tag{11}$$

$\phi_2 := \phi_2(p_{ij}, \lambda, \epsilon_2)$ acts as shock switch and $\phi_4 := \phi_4(\epsilon_2, \epsilon_4, \lambda)$ guarantees stability of the scheme in smooth regions. The coefficients are computed from pressure ratio p_{ij}, convective eigenvalues λ and constant coefficients $\epsilon_2 = 1/2$ and $\epsilon_4 = 1/64$. (10) is displayed simplified in contrast to the one used in TAU which further includes scaling factors for $\phi_{2,4}$ to increase robustness. (11) represents an undivided Laplacian from conservative variables and is evaluated over the immediate neighbors j of node i in a previous step before actual flux integration of (9) is performed.

Viscous flux $\mathbf{f}_v$ contributions are discretized in the same straightforward manner and read simplified as

$$\mathbf{f}_v \cdot \mathbf{n}_{ij} = \sum_{j \in N(i)} (\mathbf{f}_v \cdot \mathbf{n}_{ij})(\mathbf{W}_i, \mathbf{W}_j, \nabla\mathbf{W}_i, \nabla\mathbf{W}_j). \tag{12}$$

All required gradients from the flow variables $\nabla \mathbf{W}$ in (12) are computed using the Green-Gauss ansatz

$$\frac{\partial \mathbf{W}}{\partial \mathbf{x}} \approx \frac{1}{vol(\Omega_i)} \sum_{j \in N(i)} \frac{1}{2}(\mathbf{W}_i + \mathbf{W}_j)\mathbf{n}_{ij}\,|\partial\Omega|, \tag{13}$$

where $|\partial\Omega|$ is the area from domain boundary $\partial\Omega$. The last part to discretize concerns about turbulent source terms in (8). Again they are obtained similarly and can be written as

$$|\Omega_i|\mathbf{Q} := |\Omega_i|\mathbf{Q}(\mathbf{W}_i, \nabla\mathbf{W}_i) \tag{14}$$

where dependency from gradients occurs for $\mathbf{Di}(\mathbf{x}, t)$ representing diffusion and for computing the vorticity magnitude for production term $\mathbf{Pr}$, respectively. In fact, noteworthy is that turbulence models are strongly coupled to the mean flow equations, for further details see [19]. Hence, the discretized control volumes Ω do not depend on time anymore because their quantities are evaluated once at the beginning of the flow simulation in a preprocessing step.

Time discretization is based on Jamesons's [18] dual-time stepping scheme for solving the unsteady Navier-Stokes equations. Using an implicit multistep discretization in time, a large set of nonlinear equations is formed and marched to steady state in pseudo time using an agglomerated multi-grid algorithm [21] within each physical time step. Preserving a time accurate conservative scheme the term $\mathbf{W}\,\dot{\mathbf{x}} \cdot \mathbf{n}$ from (8) is approximated using a discrete geometric conservation law (GCL) [8, 22] approach.

2.3 Linearization of the discretized system

The unsteady governing equations (2) of a fluid, discretized in space with a finite volume method can be written in a *semi-discrete form*:

$$\frac{\mathrm{d}}{\mathrm{d}t}\left(\mathbf{M}(\mathbf{x}, \dot{\mathbf{x}})\mathbf{W}(\mathbf{x}, \dot{\mathbf{x}})\right) + \mathbf{R}(\mathbf{W}(\mathbf{x}, \dot{\mathbf{x}})) = 0 \tag{15}$$

where residual $\mathbf{R}$ is a function of the flow solution $\mathbf{W}(\mathbf{x}, \dot{\mathbf{x}})$ dependent on grid coordinates $\mathbf{x} := \mathbf{x}(t)$ and $\dot{\mathbf{x}} := \dot{\mathbf{x}}(\mathbf{x}(t))$ are grid point velocities. Integrating (2) a diagonal matrix $\mathbf{M}$ appears in (15) which consists of

$$\mathbf{M} := diag(|\Omega_i(t)|), \;\; i = 0, ..., N\,, \tag{16}$$

and N is the number of control volumes.

By assuming the unsteady motion has a small amplitude, it is possible to decompose the unsteady terms above into a steady mean state and a small perturbation. Neglecting higher order terms $O(\Delta\mathbf{x}^2)$, the final expression for the state variables $\mathbf{W}$ dependent on grid point coordinates $\mathbf{x}$ and grid point velocities $\dot{\mathbf{x}}$ will be:

$$\mathbf{W}(\mathbf{x}, \dot{\mathbf{x}}) \approx \overline{\mathbf{W}}(\bar{\mathbf{x}}, \dot{\bar{\mathbf{x}}}) + \widetilde{\mathbf{W}}(\mathbf{x}, \dot{\mathbf{x}}), \qquad \|\widetilde{\mathbf{W}}\| \ll \|\overline{\mathbf{W}}\| \tag{17}$$

$$\mathbf{x} \approx \bar{\mathbf{x}} + \tilde{\mathbf{x}}, \tag{18}$$

whereby the grid velocities $\dot{\mathbf{x}}$ are defined as:

$$\frac{\mathrm{d}\mathbf{x}}{\mathrm{d}t} = \dot{\mathbf{x}}(t) = \dot{\bar{\mathbf{x}}}(t) \tag{19}$$

and $\overline{\mathbf{W}}, \bar{\mathbf{x}}$ indicate the mean state and $\widetilde{\mathbf{W}}, \tilde{\mathbf{x}}$ the perturbation.

Moreover, expressing the perturbations as Fourier series

$$\widetilde{\mathbf{W}} = Re\left(\sum_{n=1}^{\infty} \widehat{\mathbf{W}}_n e^{in\omega t}\right), \ \widehat{\mathbf{W}}_n \in \mathbb{C}$$
$$\tilde{\mathbf{x}} = Re\left(\sum_{n=1}^{\infty} \hat{\mathbf{x}}_n e^{in\omega t}\right), \ \hat{\mathbf{x}}_n \in \mathbb{C},$$

with ω denoting the base angular frequency and Re the real part operator, (15) can be transformed into the frequency domain, obtaining a separate linear system of equations for each harmonic. From this point we focus without loss of generality on harmonic $(n = 1)$ perturbations of the system. Therefore, given a Fourier coefficient for the grid motion represented by $\hat{\mathbf{x}}$, the Fourier coefficient of the fluid motion may be found by solving:

$$\left(i\omega\mathbf{M} + \frac{\partial \mathbf{R}}{\partial \mathbf{W}}\right)\widehat{\mathbf{W}} = -\left(\frac{\partial \mathbf{R}}{\partial \mathbf{x}} + i\omega\left(\frac{\partial \mathbf{R}}{\partial \dot{\mathbf{x}}} + \overline{\mathbf{W}}\frac{\partial \mathbf{M}}{\partial \mathbf{x}}\right)\right)\hat{\mathbf{x}}. \tag{20}$$

The accuracy of the result will depend on the degree to which the assumptions of small perturbations and linearity are satisfied. Hence a real time-dependent nonlinear system has been reduced to a single complex linear system using the assumptions of small harmonic perturbations.

3 DYNAMIC DERIVATIVES FOR UNSTEADY MOTIONS

To give an overview of aerodynamic and flight mechanical relations of periodic movements the resulting derivatives are briefly discussed with sketch in Figure 1. Lift and pitching moment are

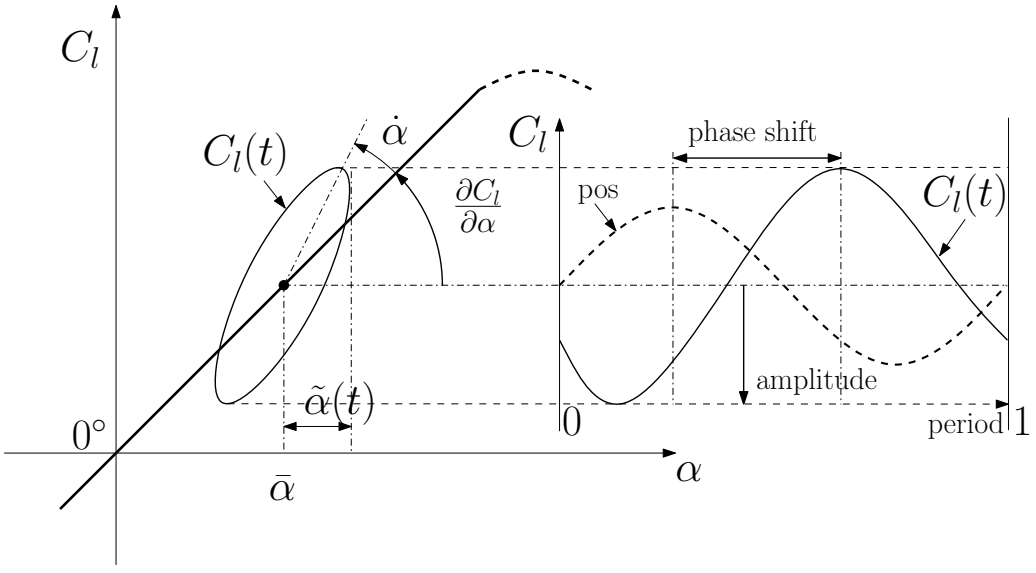

Figure 1: Appearance of dynamic derivatives $\dot{\alpha}$ (*phase shift*) and *amplitude* while performing a forced harmonic oscillation (pos) around initial angle of attack $\bar{\alpha}$.

expressed as functions of the excitation of the aircraft structure. The drag will not be considered because of its nonlinear behavior [7, 28] and small influence to the aeroelastic system. Figure 1 indicates on the left hand side a lift force polar over angle of attack, thick solid line. At the

beginning the function is affine linear and becomes at maximum lift nonlinear. After the polar has reached the maximum, the lift experience a sudden drop. Secondly, on the right hand, performing a forced harmonic motion depicted for one period marked with *pos*, around initial angle of attack $\bar{\alpha}$ will result in a phase shifted harmonic response for lift $C_l(t)$ with a certain amount of amplitude.
Furthermore, the dynamic response of lift $C_l(t)$ described by *phase shift* and *amplitude* results in an ellipsoidal curve for first harmonic oscillations seen in the lift polar plot. This behavior is similar for rolling, pitching and yawing moment. In case of moments, a further feature can be found out. The direction of rotation of the curve decides between stable or unstable motion which directly relates to positive and negative stability.
So basically all emphasis is taken to evaluate *phase shift* and *amplitude* accurately. Recent results for a two-dimensional transonic viscous test case, provided by [31], has shown good agreement for a wide range of frequencies in comparison to time accurate unsteady simulations. Finally to describe the unsteadiness of harmonic motions an often used similarity parameter, called reduced frequency k, is defined as:

$$k = \frac{\omega\, l_{ref}}{U_\infty} = \frac{2\pi f\, l_{ref}}{U_\infty} \tag{21}$$

with the angular velocity ω, the free-stream velocity U_∞, frequency f and the root chord length as reference length l_{ref}. The harmonic motion imposed is described by

$$\begin{aligned} \text{pitch: } \alpha(\tau) &= \bar{\alpha} + \tilde{\alpha} \cdot sin(k \cdot \tau) \\ \text{dimensionless time: } \tau &= \frac{U_\infty t}{l_{ref}}. \end{aligned} \tag{22}$$

Throughout the validation results section for subsonic and transonic flows one specific reduced frequency $k = 0.068$, one mean angle of attaac at 0° and two different pitch motion amplitudes, subsonic $4.52°$- transonic $0.5°$are applied.

4 THREE DIMENSIONAL VISCOUS DLR F12 WIND TUNNEL MODEL

In order to improve the accuracy of the experimental and numerical methods used for prediction of dynamic derivatives, systematic investigations have been performed using the new lightweight model DLR F12. Several sequences of experimental test series in subsonic flow conditions were undertaken to accurately predict dynamic derivatives and to understand the unsteady behavior in more detail. The wing is composed of generic NACA0012 sections to account for basic information about unsteady flow field behavior.

Table 1: Mach number and frequency range for DLR F12 configuration using reduced frequency of 0.068 and reference chord of $l_\mu = 0.253$

Ma [1]	U_∞ [m/s]	Re [1]	f [Hz]
≈0.205	70	1.28	3
0.85	289.8	5	12.4

All numerical simulations are based on unsteady Reynolds Averaged Navier-Stokes equations (URANS) to consider transient and viscous effects.

Table1 summarizes the flow conditions for two distinct simulations to be examined for validation purposes. At the beginning, experimental, URANS and LFD results will be compared for subsonic conditions in order to emphasize on the accuracy for the LFD method. Concluding with transonic conditions to point out the applicability for a wide range of flow conditions. Unfortunately, there are no experimental data for transonic conditions available.

4.1 Investigation of experimental, URANS and LFD results for DLR F12 model

Experiments were performed at the German-Dutch wind tunnel DNW-NWB in Braunschweig which is a closed-circuit low speed wind tunnel of atmospheric type. The DLR-F12 model

Figure 2: Testing facilities of the DLR F12 model in the NWB wind tunnel at Braunschweig.

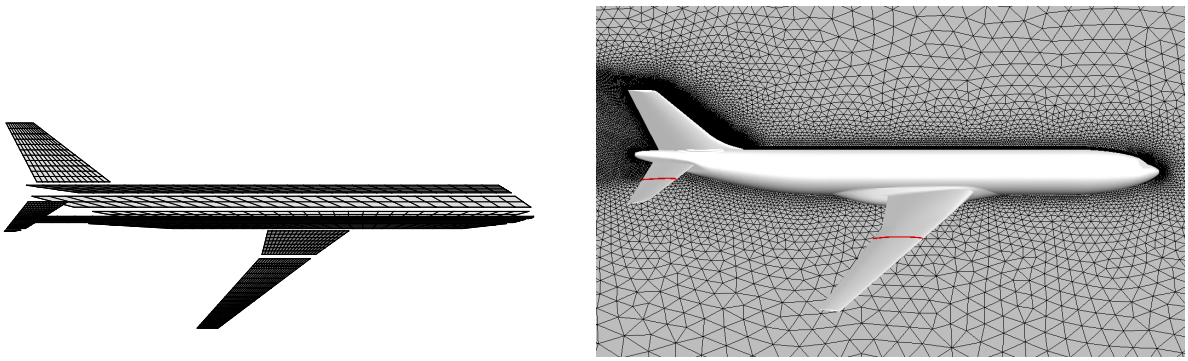

(a) DLM grid (b) CFD grid

Figure 3: Computational grids used for DLM (left) approach and CFD-LFD (right) simulations for $U_\infty = 70\,m/s$ and Re=1.28 million. In addition left figure shows the cut planes used for pressure distribution analysis at 45% of the wing span and at 46% of the horizontal tail plane span.

is a generic transport aircraft configuration designed for dynamic unsteady tests. It has a span of $b = 2.036\,m$, a reference chord of $l_\mu = 0,253\,m$ and a fuselage length of $l = 2.238\,m$. It is of modular design and made of carbon fiber sandwich construction. The models weight is approximately 12 kg and permits the measurement of steady and unsteady forces, moments and pressure distributions.

The model was mounted with a ventral sting onto NWB's MPM - Model Positioning Mechanism. The MPM can be described as a 6-Degree-of-Freedom (DOF) parallel kinematics system incorporating six struts of constant length whose joints at the wind tunnel fixed side connect to six electric linear motors. The MPM has been in operation since 2004 and is located above the test section. The MPM with the F12 model installed is shown in Figure 2(a). More details concerning the MPM can be found in Ref.[4, 13].
Through wind tunnel experiments the frequency $f = 3\,Hz$, with period length $T = 0.333\,s$, free stream velocity $U_\infty = 70m/s$, pitching amplitude of $4.52°$ and reference chord l_μ reduced frequency k is determined to be 0.068. Time-accurate simulations are performed with 100 steps per period and 1000 inner iteration per physical time step yields a physical time step size of 0.00333 seconds per step. Generally, to properly use the dual time stepping method further investigation are necessary to search for proper time step sizes and adequate amount of inner iterations. Controlling parameters for unsteady simulations were set based on previous investigations made for that model found in Ref. [12]. Finally, two periods are performed to account for a sufficient transient phase.
The computational grid around the half model, Figure 2(b), contains 11.82 million points with 18.1 mill. prisms for the boundary layer resolution and 15.1 mill. tetrahedrons for the remaining flow field. It consists of several viscous wall panels, a symmetry plane (only pitching motion) and a circular far field with a diameter of about 15 times the chord length l_μ.

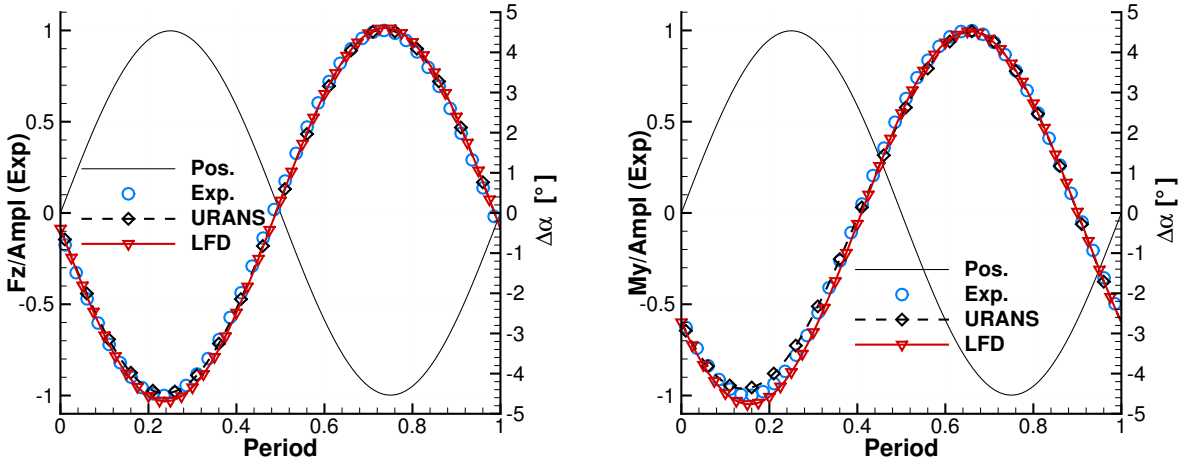

(a) Lift

(b) Pitching moment

Figure 4: Dynamic response data from LFD for DLR F12 configuration for one period with $U_\infty = 70m/s$, $Re = 1.28$ million, $\bar{\alpha} = 0.0°$, $\tilde{\alpha} = 4.52°$ and $f = 3$ Hz in comparison with experiment and unsteady simulation.

Comparison of experimental data with URANS and LFD results can be seen in Figure 4. Depicted is one period of a forced harmonic oscillation marked as *pos* with a pitch amplitude of $\tilde{\alpha} = 4.52°$ for lift (left) and pitching moment (right) response. The dynamic response data from the experiment (scattered circles) match well with URANS and LFD data. Noticeable is the small offset from URANS and LFD in the first half of the period. Unfortunately, it seems that the transient phase for the unsteady simulation was not complete and in the second half of the period all result overlap each other. Most important is that URANS and LFD results match because the LFD is derived directly from nonlinear equations used for URANS. The LFD achieves the same accuracy.

4.2 Comparison with Doublet-Lattice method

Throughout many years of development and continuous usage of Doublet-Lattice methods (DLM) it became a reliable and mature technique for aeroelastic analysis. With an in house version of this method it is possible to perform a comparison with results obtained by URANS and LFD. The grid used for the DLM approach is depicted at left in Figure 3. Only the wing and horizontal tail plane (HTP) surface were taken into account for evaluation of results. It should be stated that the DLM method provides the difference of real and imaginary part of pressure coefficient between upper and lower side at wing and HTP. So URANS and LFD results were remodeled to be presented in the same manner.
Figure 5 shows results between DLM, URANS and LFD at two representative span wise cuts on the wing at 45% span and on the HTP at 46% span. All comparisons are related to time domain simulation. Time and frequency domain solutions match well as expected for that subsonic case. The DLM results seem to indicate a small offset but the quality of the pressure distribution difference is astonishing in relation to both RANS based methods. Not only that DLM is based on the potential theory it further creates comparable results to time domain simulation and delivers results in an amazingly short time additionally. For a better visual comparison both RANS based methods are presented in Figure 6 at the same span wise cuts. Mean C_p, especially at the wing section in Figure 6(left) and slightly smoother for the HTP in (right) appears a highly visible unsteadiness in the nose region. Irrespectively of the low frequency of 3 Hertz, the incidence amplitude of 4.52° imposes a strong movement of the suction and pressure region.
Moreover Figure 6 displays the real and imaginary part of the pressure distribution (C_p) over same slices at wing and HTP for subsonic CFD conditions.
All four Figure 6(c-f) show an excellent agreement with the URANS simulation and is considered as a successful validation of the accuracy of the LFD approach. By theory, subsonic regime represents the linear flutter boundary region and the surrogate approach suppose to match with time accurate unsteady results.

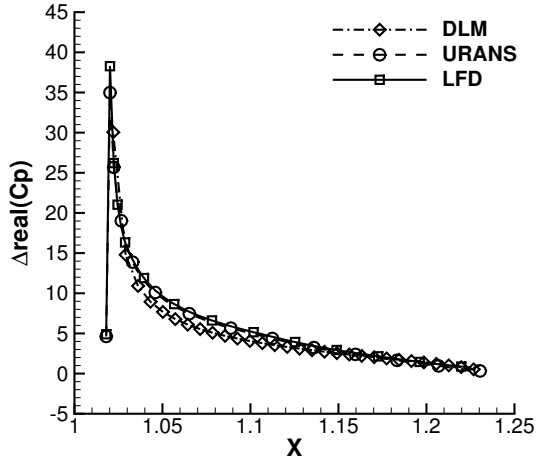

(a) ΔC_p^{real} at 45% wing span

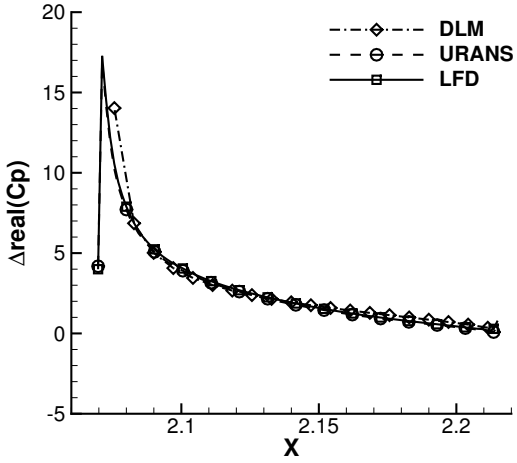

(b) ΔC_p^{real} at 46% HTP span

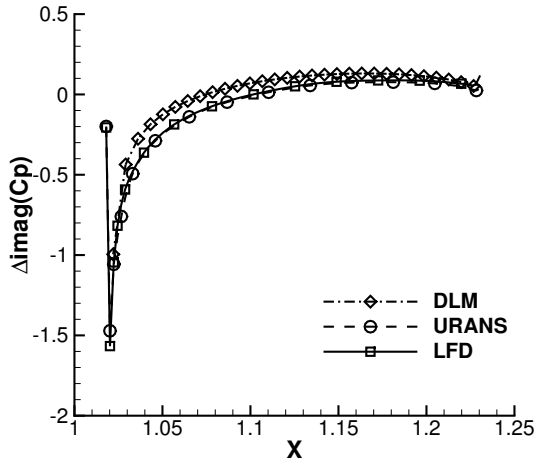

(c) ΔC_p^{imag} at 45% wing span

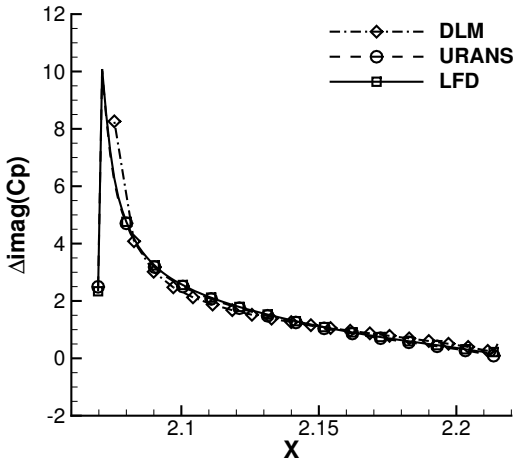

(d) ΔC_p^{imag} at 46% HTP span

Figure 5: Real and imaginary part of surface pressure distribution at wing (left) and HTP (right) for DLM, URANS and LFD. DLR F12 configuration with $U_\infty = 70m/s$, $Re = 1.28$ million, $\bar{\alpha} = 0°$, $\tilde{\alpha} = 4.52°$ and $f = 3$ Hz.

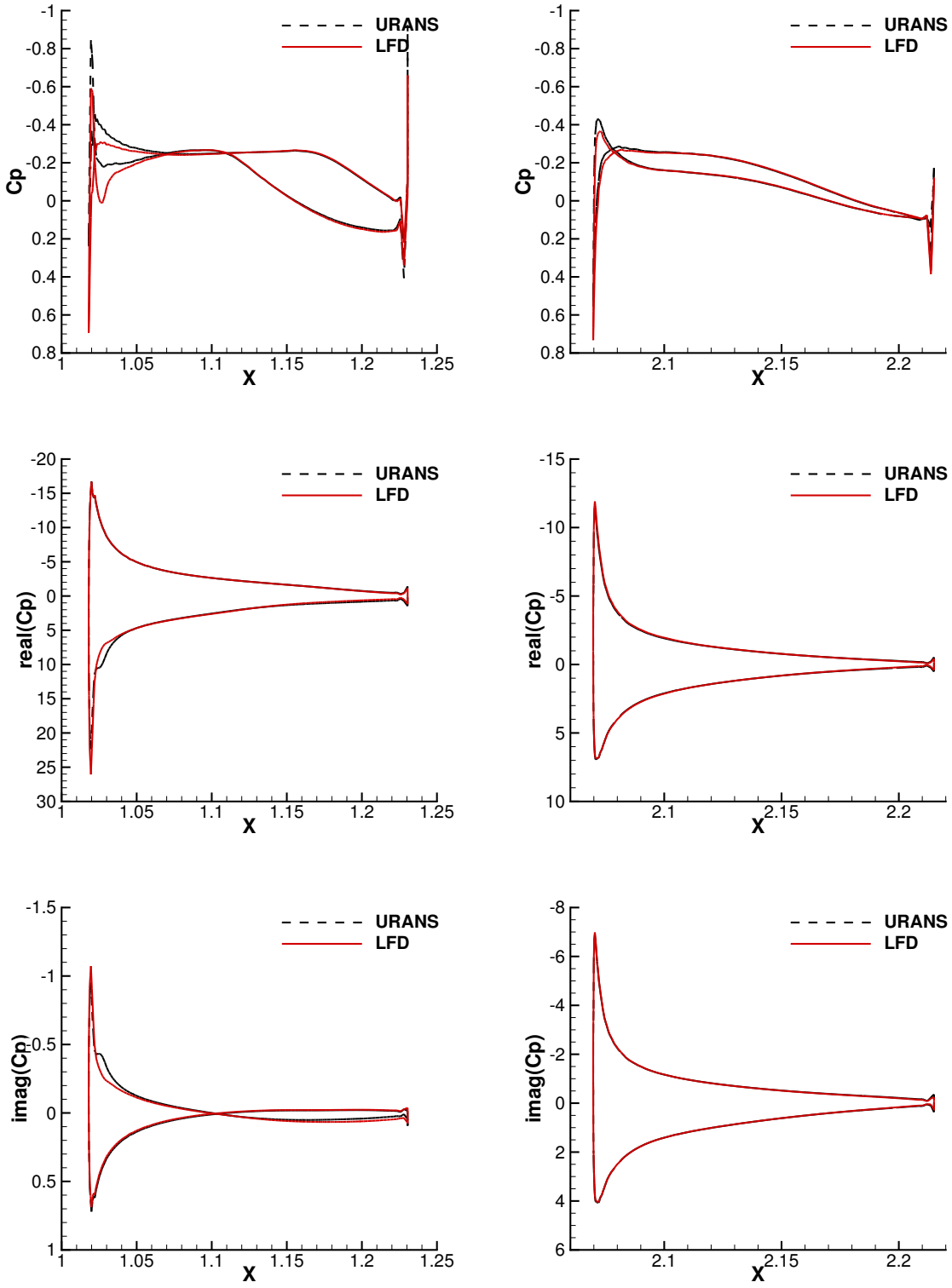

Figure 6: Mean, real and imaginary part (from top to bottom) of surface pressure distribution at 45% wing span (left) and 46% HTP span (right) for DLR F12 configuration with $U_\infty = 70m/s$, $Re = 1.28$ million, $\bar{\alpha} = 0$, $\tilde{\alpha} = 4.52°$ and $f = 3$ Hz.

4.3 Dynamic derivatives - subsonic case

Calculated real and imaginary part, amplitude and phase shift for first harmonic of lift and pitching moment for DLM, time-domain (URANS) and frequency-domain (LFD) are depicted in Table 2. First harmonics from lift and pitching moment between URANS and LFD have

Table 2: Comparison of dynamic derivatives for lift (top) and pitching moment (bottom) derived from DLM, URANS and LFD for viscous subsonic DLR F12 simulation.

Simulation	Real [1]	Imag [1]	Amplitude [rad]	Phase [rad/s]
DLM	6.081	0.292	6.088	0.0480
URANS	5.798	0.411	5.812	0.0708
LFD	5.720	0.432	5.741	0.0749
DLM	-2.037	-1.240	2.385	-2.595
URANS	-2.434	-1.617	2.922	-2.554
LFD	-2.378	-1.612	2.877	-2.548

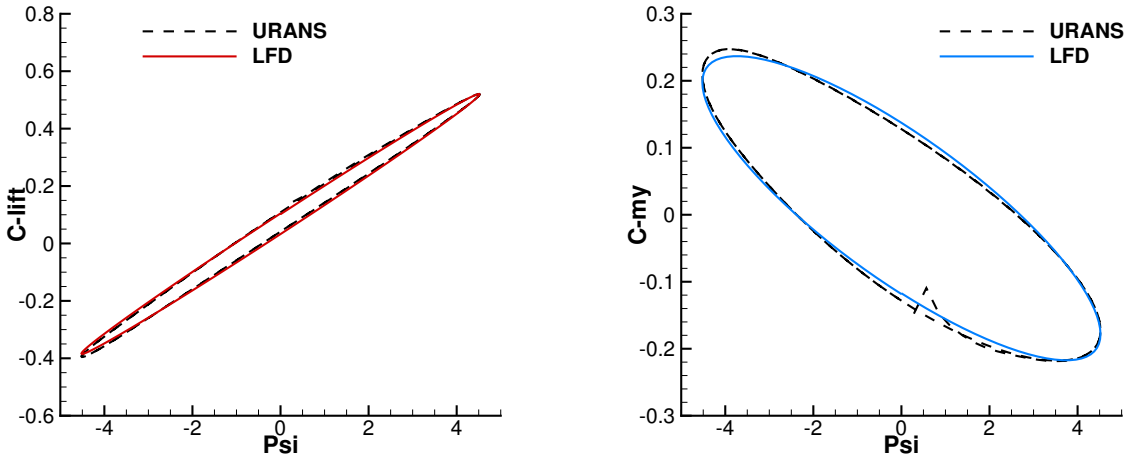

(a) C_l (b) C_{my}

Figure 7: Dynamic response data for lift and pitching moment for DLR F12 configuration with $U_\infty = 70m/s$, $Re = 1.28$ million, $\bar{\alpha} = 0.0°$, $\tilde{\alpha} = 4.52°$ and $f = 3$ Hz.

small deviations only. As an example phase shift for pitching moment has a difference of 0.006 rad/s which appears to be less then 1° off. Amplitudes for lift and pitching moment are 1.2% and 1.6% off in relation to URANS. This accuracy is of particular advantage for many aeroelastic investigations. Obtained DLM results are difficult to compare because wing and HTP are the only surfaces which are taken into account. Nevertheless, the overall close quantity to RANS methods is astonishing.

As a further comparison Figure 7 visualizes the hysteresis response for lift and pitching moment obtained from both numerical approaches. Contrary to exhaustive computation time and apart from individual numerical models, URANS has one incredible advantage to provide correct physical responses. It is seen notably for pitching moment and much less for lift that higher

harmonics take place. Both dynamic responses from URANS have no pure ellipsoidal shape. Mainly caused by the forced motion with a pitch amplitude of 4.52°. Although there are higher harmonic fractions included, the first harmonic is predicted with sustainable accuracy.
Overall, validation results for this subsonic test case show a good agreement with experimental and unsteady data and thus makes the LFD an ideal supplemental tool for further investigations of flight dynamic envelopes.

4.4 DLR F12 pitching oscillation - transonic viscous

A very important application for the linearized method is their applicability in the transonic regime. In case of flutter analysis, prediction of the sharp drop within the flutter boundary is crucial for further investigations and industrial relevance. Now, same steps as outlined for subsonic investigation are conducted at a Mach number of 0.85 for the DLR F12 configuration. It is exceptionally from interest because the appearance of nonlinear flow effects will have a significant influence on URANS and presumably LFD computations. That means especially for LFD it must be proved that computational time and robustness, by solving a linear system of equations, is satisfactory.
Flow conditions are set to be at an equal altitude, mean sea level, and constant temperature. Hence, the Reynolds number increases to approximately 5 million. This leads to a remodeling of the computational grid to encounter for the smaller boundary layer thickness. After corrections the grid consists of 11.44 million grid points with 17.35 million prisms for the boundary layer resolution and 15.03 million tetrahedrons for the far field region.
Introducing the same unsteadiness by a reduced frequency of 0.068 the frequency increases to about 12 Hertz, see Table 1. That results in a time per period of $T = 0.08067\,s$. Transonic URANS includes again 100 steps per period with 1000 inner iterations per physical time step. One physical time step is then 0.000807 seconds. Now, four complete periods are calculated to get over the transient phase. Unfortunately, there are no experimental data available for this transonic case.
Mean pressure distribution for URANS and steady pressure distribution used for LFD are depicted in Figure 8 first row, for wing (left) and for HTP (right). The wing exhibits a strong shock on the lower wing side, where small deviations between the two pressure distributions can be observed. On the upper side of the wing - at the beginning of the shock - there is another slight deviation. The causes are still not clear but one reason may be separation. In relation, the HTP data matches better for both approaches as expected. Consider that the HTP is not addicted to a shock system for that transonic flow conditions. Questionable is the HTP's movement. The pitching axis is positioned at the center of gravity near the wings aerodynamical center. This forces the HTP in a pitching and heaving motion. Recalling the linear system for LFD, the right hand side (20), introduces deformation modes. For this case a pure pitching mode is outlined.
The wing's real and imaginary pressure distributions depictes for LFD large overshoots as seen on the left Figure 8. However the peaks from the LFD are aligned horizontally with the peaks from the URANS simulation. From that it can be concluded that no phase shift appears. Table 3 summarizes dynamic response data for first harmonics for URANS and LFD calculations. Contrary to visible differences in Figure 8 for C_p distributions, integral force and moment yield barely to no deviation. Amplitudes for wing and HTP are less than 1 percent off. Phase shift for wing is around 2.4 degree and difference between both are neglectable. HTP's phase shift offset is about 0.3 degree and is well within computational margins. Finally, Figure 9 displays the hysteresis response for lift and pitching moment for both numerical approaches. Lift and

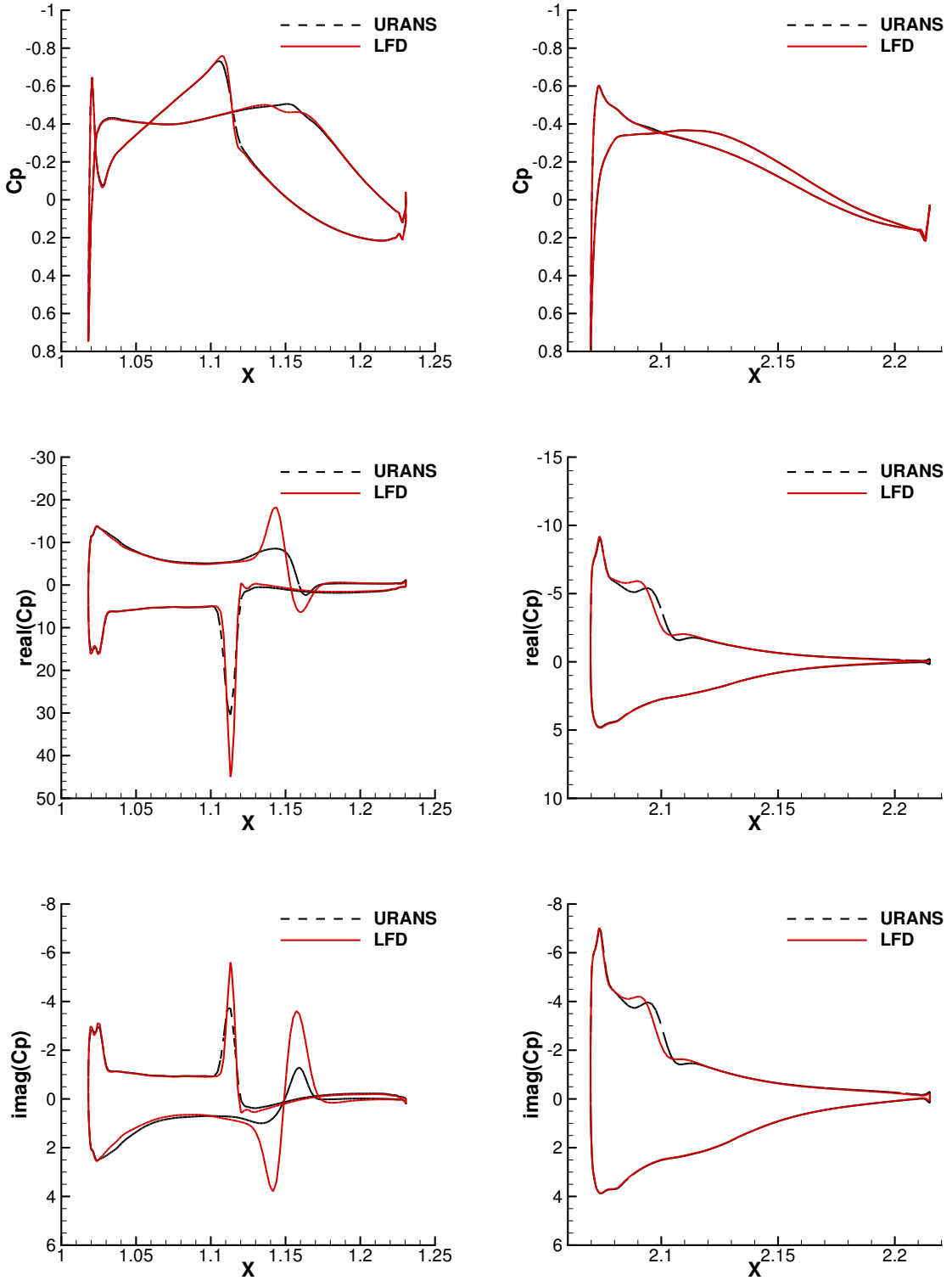

Figure 8: Mean, real and imaginary part (from top to bottom) of surface pressure distribution at 45% wing span (left) and 46% HTP span (right) for DLR F12 configuration with $Ma = 0.85$, $Re = 5$ million, $\bar{\alpha} = 0°$, $\tilde{\alpha} = 0.5°$and $f = 12.3$ Hz.

pitching moment represent a purely first harmonic oscillation noticeable by the elliptic shape. It is often observed that the pitching moment in transonic flows has non negligible contributions

Table 3: Comparison of dynamic derivatives for lift (top) and pitching moment (bottom) derived from URANS and LFD for viscous transonic DLR F12 simulation.

Simulation	Real [1]	Imag [1]	Amplitude [rad]	Phase [rad/s]
URANS	8.9886	-0.3779	8.9966	-4.202e-2
LFD	8.9439	-0.3794	8.9519	-4.239e-2
URANS	-3.8617	-2.4282	4.5619	-2.580
LFD	-3.8572	-2.4007	4.5436	-2.585

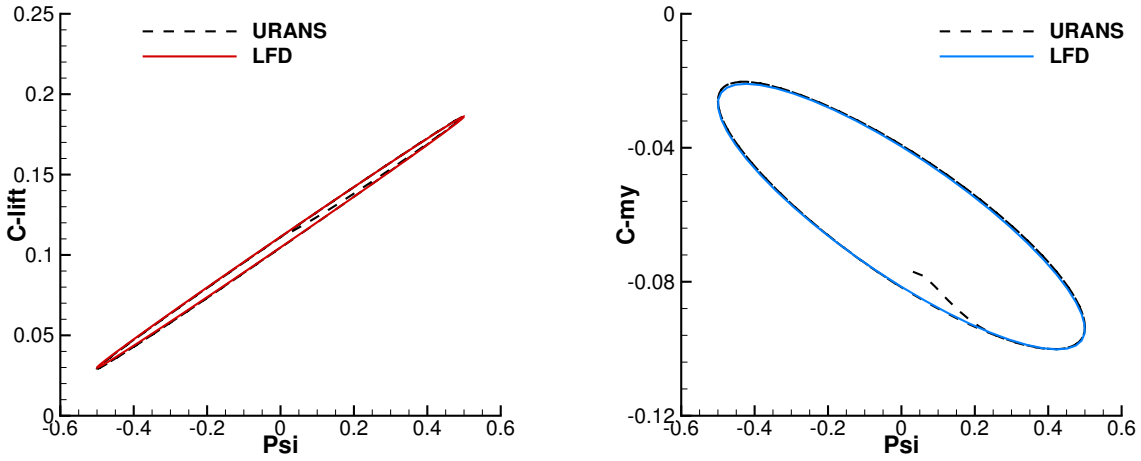

(a) Lift

(b) Pitching moment

Figure 9: Dynamic response data for lift and pitching moment for DLR F12 configuration with $Ma = 0.85$, $Re = 5$ million, $\bar{\alpha} = 0.0°$, $\tilde{\alpha} = 0.5°$and $f = 12.4$ Hz.

of higher harmonics. However, this nonlinearity is avoided due to the small pitch amplitude of $\tilde{\alpha} = 0.5°$.

4.5 Time consumption in comparison to different approaches

One of the key-issues of the LFD solver is the computational performance in comparison to unsteady time accurate simulations. During the validation process time measurements were made to emphasize the possible time reduction for Navier-Stokes (URANS, LFD) computations. Table 4 presents the time consumption and efficiency for all test cases in use. As a reference for the time factor the RANS simulation was chosen. LFD time factors in relation to URANS are shown in brackets. Computation times depicted correspond to a single processor. Wall clock times were multiplied by the number of processors. URANS and LFD simulations were executed with 32 and 96 processors, respectively on a Linux cluster system. The minimal residual for the DLM in Table 4 is signposted as ∞ because the system of equations are solved directly with one step.
Achieved minimal residual for steady simulations (RANS) are pointed out to highlight the importance to be well converged which minimizes the error introduced for LFD applications. URANS is based on dual time stepping and does not need such a well converged RANS restart

Table 4: Computational effort in hours (h) and time factors for subsonic (top) and transonic (bottom) flows for DLR F12 configuration were p is the number of periods simulated for URANS.

Simulation	Time [h]	min. Residual	time factor
DLM	0.16 h	∞	0.00028
RANS	569 h	2.9e-8	1
URANS	9540 h (p=2)	$\approx$1e-3	16.8
LFD GMRes	446 h	7.7e-5	0.78 (21.5)
RANS	682 h	1.4e-6	1
URANS	10.848 h (p=4)	$\geq$ 1e-1	15.9
LFD GMRes	816 h	2.3e-5	1.2 (13.3)

Table 5: Actual computational effort in hours (h) and time factors using approximately the same load factors for URANS and LFD for DLR F12 configuration were p is the number of periods simulated for URANS.

Test case	URANS [h]	LFD [h]	# proc	time factor
subsonic	270(p=2)	4.6	32/96	$\approx$59
transonic	339(p=4)	8.5	32/96	$\approx$40

solution usually.
When switching from subsonic into transonic flow regimes the DLR F12 LFD simulation exhibits a decreased time reduction factor. In parallel, LFD's communication is increased dramatically by solving the double solution vector and for viscous cases the convergence rate does not behave similarly to the steady simulation anymore. An agglomerated multi grid technique is applied for solving the complex valued linear system. For viscous cases, including turbulence derivatives, robustness should not be underestimated. In fact, convergence often stalls or diverge. Improving the robustness with turbulence derivatives a GMRes [27] accelerator in conjunction with multi grid can be selected. Applying GMRes was indispensable and has raised the number of processor to 96 instead of 32 for RANS and URANS, Table 5. All that increases computational time and memory usage dramatically but neglecting the influence of turbulence with increasing Mach number can lead to seriuosly wrong results [31].

5 CONCLUSIONS

An efficient linear solver for predicting unsteady aerodynamic data has been described and demonstrated for viscous, subsonic and transonic flows. It can serve as a powerful alternative tool for aeroelastic applications. This approach was validated in comparison with experimental data and a time accurate unsteady simulation for the subsonic three dimensional DLR F12 wind tunnel model. Emphasizing the accuracy for a frequency of 3 Hertz and a large pitch amplitude of 4.52 degree.
Even the appearance of higher harmonic fractions for dynamic responses do not distort the result significantly. An important outcome to note especially for pitching moments: because little in advance can be said whether it will remain pure first harmonic or will include higher harmonics additionally. It is less severe for lift which remains mostly linear.

Simulations at transonic flow conditions with a complex shock system for the DLR F12 model shows the maturity of the method for application in real aircraft flutter analysis. Well comparable accuracy between URANS and LFD has proven the applicability of the LFD for a wide range of Mach numbers, establishing the LFD as a serious exchange for the costly URANS simulations.
Apart from that, investigations in the transonic regime have realized once again the difficulties to obtain meaningful time accurate solutions. Whenever strong shocks and flow separation appears increased time effort and numerical experience is needed for a successful unsteady computation. In contrary linear system based LFD simulations have converged always until amplitudes and phase shift stagnated. Residual drops of 5 to 6 magnitudes were common. However, no convergence for LFD was reached if reduced frequencies are set above 0.2.
Nevertheless, the time savings generated by the LFD instead of URANS range up to one order of magnitude for all test cases. Particularly that time reduction is favorable for the huge parameter space which has to be covered.

ACKNOWLEDGEMENTS

The first author acknowledges the support by the European project ALEF in which we have benefited from many discussion and to be able to perform numerical simulations with the DLR F12 configuration.

REFERENCES

[1] Edward Albano and William P. Rodden. A Doublet-Lattice method for calculating lift distributions on oscillating surfaces in subsonic flows. *AIAA Journal*, 7(2):279 – 285, February 1969.

[2] Ken J. Badcock, Sebastian Timme, S. Marques, H. Khodaparast, M. Pradina, J.E. Mottershead, A. Swift, Andrea Da Ronch, and M.A. Woodgate. Transonic aeroelastic simualtion for instability searches and uncertainty analysis. *Progress in Aerospace Sciences*, 47:392 – 423, 2011.

[3] Oddvar O. Bendiksen and Kenneth A. Kousen. Transonic flutter analysis using the Euler equations. In *Structural Dynamics and Materials Conference*, number AIAA-87-0911 in Presented at the AIAA - ASME/ ASCE/AFIS 28th Structures, Monterey, CA, April 6-8 1987.

[4] Andreas Bergmann, Andreas Rene Hübner, and Thomas Löser. Experimental and numerical research on the aerodynamics of unsteady moving aircraft. *Progress in Aerospace Sciences*, **4**4:121–137, 2008.

[5] G. Brendes and Ralph Voß. Transonic flutter calculations for a low wing transport aircraft using the transonic Doublet Lattice method. In *IFASD, Madrid/Spain, June 5-7 2001*, 2001. LIDO-Berichtsjahr=2001,.

[6] Earl H. Dowell. Some recent advances in nonlinear aeroelasticity: fluid-structure interaction in the 21st century. *AIAA-2010-3137*, 2010.

[7] B. Etkin. *Flugmechanik und Flugregelung*. Berliner Union Stuttgart, 1966.

[8] Charbal Farhat, Philippe Geuzaine, and Celine Grandmont. The discrete geometric conservation law and the nonlinear stability of ale schemes for the solution of flow problems on moving grids. *Journal of Computational Physics*, 174(2):669–694, 2001.

[9] D. H. Fuglsang and M. H. Williams. Non-isentropic unsteady transonic small disturbance theory. *AIAA Paper 85-0600*, 1985.

[10] J. P. Giesing, T. P. Kalman, and William P. Rodden. Direct application of the nonplanar Doublet Lattice method. *AIAA Journal*, I(AFFDL-TR-71-5):279–285, February 1971.

[11] Kenneth C. Hall, William S. Clark, and Christopher B. Lorence. Linearized Euler analysis of unsteady transonic flows in turbomachinery. *Journal of Turbomachinery*, 116(3):477–488, 1994.

[12] Andreas Rene Hübner. Experimentelle und numerische Bestimmung der dynamischen Derivative. FB 2009-26, DLR, 2009.

[13] Andreas Rene Hübner, Andreas Bergmann, and Thomas Löser. Experimental and numerical investigations of unsteady pressure distributions and aerodynamic forces on moving transport aircraft configurations. In *47th AIAA Aerospace Sciences Meeting*, volume AIAA-2009-0091, Orlando, Florida, 2009.

[14] U. Iemma and M. Gennaretti. Reduced-order modeling for linearized aeroelasticity of fixed wings in transonic flight. *Journal of Fluids and Structures*, 21(3):243 – 255, 2005.

[15] Koji Isogai. On the transonic-dip mechanism of flutter of a sweptback wing. *AIAA Journal*, 17(7):793 – 795, 1979.

[16] Koji Isogai. Numerical study of transonic flutter of a two-dimansional airfoil. Technical Report NAL TR-617T, JAXA, CHOFU, Tokyo, Japan, 1980.

[17] Anthony Jameson, Wolfgang Schmidt, and Elias Turkel. Numerical solutions of the Euler equations by finite volume methods using Runge-Kutta time-stepping schemes. *AIAA Paper 81-1259*, 1981.

[18] Antony Jameson. Time dependent calculations using multigrid, with applications to unsteady flows past airfoils and wings. *AIAA Paper 91-1596*, 1991.

[19] Stefan Langer. Application of a line implicit method to fully coupled system of equations for turbulent flow problems. *Journal of Computer and Fluids*, page DOI: 10.1002/fld2561, 2011.

[20] Michel Lesoinne, Marcus Sarkis, Ulrich Hetmaniuk, and Charbel Farhat. A linearized method for the frequency analysis of three-dimensional fluid/structure interaction problems in all flow regimes. *Computer Methods in Applied Mechanics and Engineering*, 190(24-25):3121 – 3146, 2001. Advances in Computational Methods for Fluid-Structure Interaction.

[21] Dimitri J. Mavriplis. Multigrid strategies for viscous flow solvers on anisotropic unstructured meshes. *Journal of Computational Physics*, 145(1):141–165, 1998.

[22] Dimitri J. Mavriplis and Zhi Yang. Construction of the discrete geometric conservation law for higher-order time accurate simulations on dynamic meshes. *Journal of Computational Physics*, 213(2):557–573, April 2006.

[23] Bruno Mialon, Alex Khrabrov, Saloua Ben Khelil, Andreas Hübner, Andrea Da Ronch, Ken Badcock, Luca Cavagna, Peter Eliasson, Mengmeng Zhang, Sergio Ricci, Jean-Christophe Jouhaud, Gilbert Rogé, Stephan Hitzel, and Martin Lahuta. Validation of numerical prediction of dynamic derivatives: The DLR-F12 and the transcruiser test cases. *Progress in Aerospace Sciences*, 47(8):674 – 694, 2011.

[24] Guy Daniel Mortchéléwicz. Flutter simulations. *Aerospace Science and Technology*, 4(1):33–40, January 2000.

[25] Walter J. Mykytow. A brief overview of transonic flutter problems. CP 226, AGARD, April 1977.

[26] Alexander Pechloff and Boris Laschka. Small disturbance navier-stokes computations for low-aspect-ratio wing pitching oscillations. *Journal of Aircraft*, **4**7(**3**):737–753, 2010.

[27] Y. Saad and M. H. Schultz. GMRES: A generalized minimum residual algorithm for solving non-symmetric linear systems. *SIAM Journal of Scientific and Statistical Computing*, 7(3):856–859, 1988.

[28] Hermann Schlichting and Erich Truckenbrodt. *Aerodynamik des Flugzeuges*, volume I/II. Springer Verlag, 2nd edition, 1969/1971.

[29] Walter A. Silva and Robert M. Benett. Using transonic small disturbance theory for predicting the aeroelastic stability of a flexible wind-tunnel model. TM 102617, NASA, Langley Resaerch Center, Hampton, Virginia 23665-5225, March 1990.

[30] Philippe R. Spalart and Steven Richard Allmaras. A one-equation turbulence model for aerodynamic flows. *AIAA Paper 92-0439*, 1992.

[31] Reik Thormann and Markus Widhalm. Linear frequency domain predictions of dynamic response data for viscous transonic flows. *AIAA Journal*, Submitted and accepted for review, 2012.

[32] D.-M. Tran, C. Liauzun, and C. Labaste. Methods of fluid-structure coupling in frequency and time domains using linearized aerodynamics for turbomachinery. *Journal of Fluids and Structures*, 17(8):1161 – 1180, 2003.

[33] Markus Widhalm, Richard Patrick Dwight, Reik Thormann, and Andreas Rene Hübner. Efficient computation of dynamic stability data with a linearized frequency domain solver. In J. C. F. Pereira and A. Sequeira, editors, *Fifth European Conference on Computational Fluid Dynamics*, Lisbon, Portugal, June 14-17 2010. ECCOMAS CFD 2010.

[34] J.C. Wu, K.R.V. Kaza, and N.L. Sankar. A technique for the prediction of airfoil flutter characteristics in separated flows. In *Structural Dynamics and Materials Conference*, number AIAA-87-0910 in Presented at the AIAA[ASME/ ASCE/AFIS 28th Structures, Monterey, CA, April 6-8 1987.